Hindawi
Scientific Programming
Volume 2021, Article ID 2553244, 8 pages
https://doi.org/10.1155/2021/2553244

Research Article

Support Vector Machine Parameter Optimization for Positron Emission Tomography Images for Estimation of Recurrent Laryngeal Nerve Injury with Thyroid Nodules

Jiyuan Wang,[1] **Hanqing Zou**,[2] **Shaokun Sun**,[2] **Wenqian Xu**,[2] **and Jie Jin**[3]

[1]*General Surgery Block-9A, Suzhou Kowloon Hospital, Shanghai Jiaotong University School of Medicine, Suzhou 215028, China*
[2]*Department of General Surgery, The Second Affiliated Hospital of Soochow University, Suzhou 215004, China*
[3]*Department of General Surgery, Suzhou Ninth People's Hospital, Suzhou 215200, China*

Correspondence should be addressed to Jie Jin; 181100439@mail.dhu.edu.cn

Received 14 July 2021; Accepted 12 August 2021; Published 29 August 2021

Academic Editor: Gustavo Ramirez

This study aimed to explore positron emission tomography-computed tomography (PET-CT) images based on support vector machine (SVM) algorithm for the classification of thyroid nodules (TN) and its evaluation value in postoperative injury rate (PPIR) of recurrent laryngeal nerve (RLN). The parameters of the SVM algorithm were optimized using the particle swarm optimization (PSO) algorithm. A total of 58 patients who were diagnosed with TN by PET/CT at a hospital were divided into a group with benign nodules (group B, 25 cases) and a group with malignant nodules (group M, 33 cases). The characteristics of the PET-CT images and difference in the max standardized uptake value (SUV_{max}) of PET-CT were analyzed. The PPIR of RLN was calculated. It was found that when the number of iterations was 19, the fitness and the classification accuracy of the SVM algorithm was 98.3% and 91.1%, respectively. When $SUV_{max} = 4.56$, its sensitivity and specificity were 81.33% and 76.18%, respectively. The SUV_{max} of group B was much lower ($P < 0.01$). It indicated that the established method could realize higher classification accuracy on TN and was of great significance in the evaluation of the PPIR of RLN.

1. Introduction

TN is a common endocrine system disease second only to diabetes. The incidence rate is relatively high in middle-aged and elderly women, ranking the fifth in female malignancies. Statistics have shown that the incidence of TN has increased nearly 10 times in the past 10 years, and it is in a trend of continuous increase, with an average annual growth rate of 6.2% [1]. The pathogenesis of TN is still unclear. It can be classified into two categories: benign and malignant. Early differentiation of benign and malignant lesions is of great value for clinical diagnosis, treatment, and prognosis. In clinical work, it is found that the detection rates of these diagnostic methods can be 50%~70%, and the 69% TN is misdiagnosed as adenocarcinoma [2]. With the continuous development of medical technology, PET-CT has been widely used in the diagnosis of malignant tumors, but there is still a lot of controversy in the differentiation of benign and malignant TN. At present, the TN are mainly treated by surgery, but various complications are prone to occur after the surgery. Among them, the RLN injury is the most common and the most serious complication after the thyroid surgery. A severe RLN can cause the patient to breathe with difficulty and can even be life-threatening [3]. Many studies have shown that the PPIR of RLN in patients with benign TN is greatly lower than that of patients with malignant TN [4].

PET-CT can clearly show the location of nodules with high accuracy and precise positioning, but it is controversial in the diagnosis of benign and malignant TN [5]. As there are many types of diseases associated with thyroid, the nodules are complex and diverse, and the manifestations of PET-CT images are also more diverse. During the diagnosis, it is necessary to have a qualitative analysis by experienced doctors, which is subjective and unstable. Machine learning

in artificial intelligence (AI) technology can semiautomatically diagnose the nodules and reduce the workload and subjective influence of doctors. SVM can transform a given set of space vectors into another space with a higher dimension according to a given nonlinear mapping, and then solve the optimal classification solution in this space [6]. SVM is capable of minimizing the resolution and maximizing the generalization and has been applied to classification of cancer gene expression data, classification of isolated lung nodules in the lungs, and regression. The selection of SVM parameters is correlated with the classification and regression results [7]. However, there is no definite theory to guide the selection of parameters.

In summary, PET-CT has to be further studied for the differentiation of benign and malignant TN, and there is no clear theoretical guidance for the selection of SVM parameters. Therefore, TN patients were selected as the research objects, the SVM parameters were optimized, and a SVM optimized classification method based on the PET-CT image characteristics of TN was established in this study. It was done to explore the value of PET/CT in the differential diagnosis of benign and malignant TN and the evaluation of PPIR of RLN.

2. Materials and Methods

2.1. Research Objects and Grouping. 58 patients who had performed the PET/CT examinations at a hospital from December 2018 to April 2020 and were confirmed to have TN from pathological results were selected as the research subjects. There were 16 males and 42 females, whose age range was 22–79 years, with an average value of 61.17 ± 10.62. According to the PET-CT diagnosis results, the patients were divided into group B with benign nodules (25 cases) and group M with malignant groups (33 cases). There were 33 patients with malignant nodules and 25 patients with benign nodules. All patients underwent thyroidectomy after diagnosis. The experimental procedure had been approved by the ethics committee of the hospital, and all subjects included had signed the informed consent forms.

2.2. Establishment of the SVM Algorithm. For a given training dataset A, a set of n nodes could be expressed as

$$A = \left\{(x_i, y_i) | x_i \in R^P, y_i \in (-1, 1)\right\}_{i=1}^{n}. \tag{1}$$

In the above equation, y_i was 1 or −1, referring to the category the node x_i belonged to. Each classification surface had to meet $\omega \cdot x + b = 0$, where $\cdot$ is the dot product, ω represents the normal vector of the classification surface, and b is the spatial bias. The normal vector of the hyperplane distance was determined by $b/\|\omega\|$, and the classification interval could be expressed as $2/\|\omega\|$.

Maximizing the distance between the two classification planes could be achieved by minimizing $\|\omega\|$. To prevent the training node from falling into the boundary area of the two classification planes, each sample node i had to satisfy $\omega \cdot x + b \geq 1$ or $\omega \cdot x + b \leq -1$. Then, the classification plane could be given as

$$yi(\omega \cdot x + b) \geq 1, \quad 1 \leq i \leq n. \tag{2}$$

In summary, the optimization was mainly achieved by minimizing $\|\omega\|$, so that each node could satisfy $yi(\omega \cdot x + b) \geq 1$. A given training set was set with the pair (f_i, d_i) of feature value and grade label, where $f \in R^n$ referred to the feature value of the model. The optimization of the classification surface was transformed into a constrained optimization issue, which could be indicated as $\min \Phi(\omega) = 1/2\|\omega\|^2$. The objective of the SVM model was to solve the following optimization issues:

$$\begin{aligned} &\min_{\omega,b,\varepsilon} \frac{1}{2} W^T W + B \sum_{i=1}^{n} \varepsilon_i, \\ &\min_{\omega,b,\varepsilon} \frac{1}{2} W^T W + B \sum_{i=1}^{n} \varepsilon_i \min_{\omega,b,\varepsilon} \frac{1}{2} W^T W + B \sum_{i=1}^{n} \varepsilon_i. \end{aligned} \tag{3}$$

In the equation, B is the penalty factor for dividing the wrong term, and ω refers to a possible high-dimensional vector variable.

The classification of benign and malignant TN was a nonlinear and separable case, which could be described as

$$\begin{aligned} &\min_{\omega,b,\varepsilon} \frac{1}{2} \|\omega\|^2 + B \sum_{i=1}^{n} \varepsilon_i, \\ &y_i(\omega \cdot x_i + b) \geq 1 - \varepsilon_i, \\ &\varepsilon_i \geq 0, \quad i = 1, 2, \ldots, n. \end{aligned} \tag{4}$$

The dual solution is given as follows:

$$\begin{aligned} &\min \frac{1}{2} \sum_{i=1}^{n} \sum_{j=1}^{n} y_i y_j \mu_i \mu_j K(x_i, y_i) - \sum_{j=1}^{n} \mu_i, \\ &\sum_{i=1}^{n} y_i \mu_i = 0, \quad 0 \leq \mu_i \leq B, \; i = 1, 2, \ldots, n. \end{aligned} \tag{5}$$

In the above equation, μ_i refers to the Lagrangian coefficient, which satisfied $\mu_i > 0$, and $K(x_i, y_i)$ is the kernel function.

By introducing the kernel function $K(x_i, y_i)$, SVM could transform the inseparable data in the low-dimensional feature space into the high-dimensional, linear, and separable specialization space, and convert the nonlinear classification into the appropriate linear classification. The penalty factor B controlled the balance between the two classifications [8]. Appropriate $K(x_i, y_i)$ and parameter B were selected to solve equation (5), and then the obtained decision function was written as

$$f(x) = \operatorname{sgn}\left(\sum_{i=1}^{n} \mu_i^* y_i K(x_i, y_i) + b^* \right). \tag{6}$$

In the above equation, sgn() is the function symbol, b^* refers to the intercept of the classification function, and μ_i^* represents the optimal solution of the function.

There were many ways to express the kernel function $K(x_i, y_i)$. Among them, the radial basis function (RBF) showed better learning ability under different conditions, which was applicable for small samples with low dimensionality [9]. The RBF expression is given as follows:

$$K(x_i, y_i) = \exp\left(-\frac{|x_i - y_i|^2}{\gamma^2}\right). \quad (7)$$

In order to achieve the optimal B value and the γ value in $K(x_i, y_i)$, the PSO algorithm was introduced in this study. The PSO algorithm had the characteristics of a simple algorithm and fast convergence speed and was an efficient and practical search method [10]. The position of the i^{th} particle in the A-dimensional space could be written as $X_i = (x_{i1}, x_{i2}, \ldots, x_{iA})$, the speed was $V_i = (v_{i1}, v_{i2}, \ldots, v_{iA})$, the experienced position was $P_i = (p_{i1}, p_{i2}, \ldots, p_{iA})$, the best position was recorded as the individual extreme point gb, and the best position for each particle was $Gi = (pb_{i1}, pb_{i2}, \ldots, pb_{iA})$. For the t^{th} iteration of particle i in A-dimensional space ($1 \le d \le A$), its corresponding velocity and position could be calculated using the following equations:

$$v_{id}^{t+1} = \omega v_{id}^{t} + \sigma_1 \text{rand}_1\left(pb_{id}^{t} - x_{id}^{t}\right) + \sigma_2 \text{rand}_2\left(gb_{id}^{t} - x_{id}^{t}\right), \quad (8)$$

$$x_{id}^{t+1} = x_{id}^{t} + v_{id}^{t+1}, \quad i = 1, 2, \ldots, N. \quad (9)$$

In the above equations (8) and (9), v_{id}^{t+1} is the velocity of the particle i at the t^{th} iteration, rand_1 and rand_2 are the random numbers within $[0, 1]$, and x_{id}^{t} refers to the position of the particle i at the t^{th} iteration. pb_{id}^{t} represents the individual extreme point of the particle i at the t^{th} iteration, σ_1 and σ_2 are the learning factors, gb_{id}^{t} represents the social extreme point of particle i at the t^{th} iteration, and ω is the inertia weight value. v refers to the velocity of each dimension of the particle, satisfying $-v_{d\max} \le v \le v_{d\max}$, the position of the particle in the d-dimensional space is $[-x_{d\max}, x_{d\max}]$, and $v_{d\max} = k x_{d\max}$ $(0.1 \le k \le 1)$.

In the optimization application of complex objective functions, PSO was prone to premature convergence [11]. In order to avoid this phenomenon, the step-by-step PSO algorithm was adopted in this study. Then, the position x_{id}^{t+1} of the particle in the $t+1^{th}$ iteration is given asfollows:

$$x_{id}^{t+1} = \begin{cases} x_{1d}^{t+1}, & f\left(x_{1d}^{t+1}\right) \ge f\left(x_{2d}^{t+1}\right), \\ & f\left(x_{1d}^{t+1}\right) \ge f\left(x_{3d}^{t+1}\right), \\ x_{2d}^{t+1}, & f\left(x_{2d}^{t+1}\right) \ge f\left(x_{1d}^{t+1}\right), \\ & f\left(x_{2d}^{t+1}\right) \ge f\left(x_{3d}^{t+1}\right), \\ x_{3d}^{t+1} & \text{others.} \end{cases} \quad (10)$$

2.3. Flows of SVM Parameter Optimization Using PSO Algorithm. The PSO algorithm was utilized to optimize SVM parameters, and the specific optimization steps are shown in Figure 1. The relevant parameters of the PSO algorithm and the SVM classifier were determined first. The number of moves S was set to 0 based on the number of particles, and the samples were trained with SVM. The next step was to judge whether the termination conditions were met or not, and then the optimal parameter was outputted if the termination conditions were met; or otherwise, it was necessary to further determine whether S was 0. If $S = 0$, the position of the particle swarm was determined according to the path, so as to start the SVM training on the sample. If S was not equal to 0, the pheromone in the path should be updated, and the position of the particle swarm was moved according to the path determination probability, so as to start the loop of SVM training on the sample until the termination conditions were met.

2.4. Scanning Method of PET-CT. The patient was instructed to fast for at least 6 hours before the scan and to keep breathing calmly during the scan. The PET-CT scan parameters were defined as follows: voltage 120 kV, current 140 mA, pitch 5.0 mm, and layer thickness 5.0 mm. Image acquisition was performed in a two-dimensional mode with 5 minutes for each patient. Attenuation correction was performed on the collected images, and the number of reconstruction iterations was set to 2, and Siemens was used to fuse the images.

2.5. Observation Indicators. All the collected images were read by two experienced physicians to obtain the PET-CT density uniformity, boundary definition, nodule size, calcification, capsule, and semiquantitative index $\text{SUV}_{\max}$ for each nodule. In addition, the PPIR of RLN of the two groups of patients was counted statistically. The $\text{SUV}_{\max}$ was calculated with $\text{SUV}_{\max} = S_a/I_a/W$, where S_a is the specific activity of the lesion, I_a refers to the imaging agent injection dose, and W is the body weight.

2.6. Statistical Methods. The test data were processed using SPSS19.0 statistical software. The measurement data were expressed as mean ± standard deviation ($\overline{x} \pm s$), and the count data were indicated with percentage (%). The diagnostic efficacy between groups was compared with the χ^2 test; and receiver operating characteristic (ROC) curve analysis was employed to analyze $\text{SUV}_{\max}$ as the best critical value. $P < 0.05$ indicated statistical difference.

3. Results

3.1. Basic Information of Patients. The age, gender ratio, and nodule size of the two groups of patients were compared and analyzed, and the results are shown in Table 1. It revealed that the differences in the age, gender ratio, and nodule size of patients with benign and malignant nodules were not observable ($P > 0.05$).

3.2. Fitness and Accuracy of the SVM Algorithm. The PSO algorithm was applied for optimizing the SVM parameters and analyzing the fitness of the optimization algorithm. The

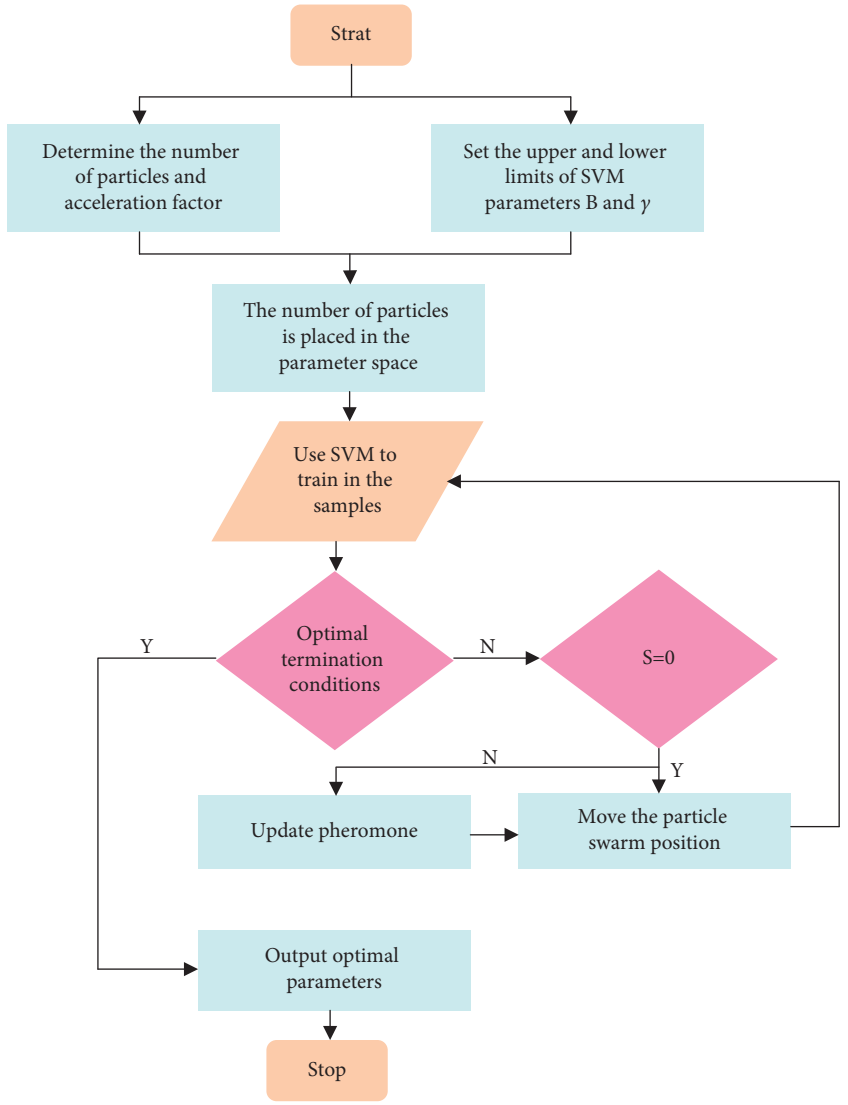

Figure 1: Flows for parameter optimization based on the SVM algorithm.

results shown in Figure 2 illustrate that as the number of iterations increased, the fitness showed an increasing trend, and the fitness level suddenly increased when the number of iterations was 19, and then remained at a stable level. During this process, the fitness level was 98.3%. Further analysis of the accuracy by taking the pathological diagnosis result as the gold standard revealed that the accuracy rate of the optimized SVM algorithm reached 89% and 95.2% for malignant and benign classification of TN, respectively. The final classification accuracy could be 91.1%.

3.3. PET-CT Images of TN Patients. The PET-CT imaging manifestations of TN were analyzed. It showed that plain CT images and enhanced CT images of patients with benign TNs were mostly irregular in shape (as shown in Figure 3). In patients with malignant TNs, the density of TN in plain CT images and enhanced CT images was uniform, and the calcifications were diverse and mostly located in the lesion (as shown in Figure 4).

3.4. Selection of Optimal Critical Values of SUV_{max}. The benign and malignant nodules for the patients included were evaluated with the SUV_{max} indicator by taking the pathological results as the gold standard. The ROC curve for SUV_{max} to diagnose TN was drawn accordingly, and the results are shown in Figure 5. It disclosed that the area under the ROC was 0.795. When $SUV_{max} = 4.56$ was undertaken as the best critical point for diagnosis, the sensitivity and the specificity of SUV_{max} in diagnosing the benign and malignant nodules was 81.33% and 76.18%, respectively.

3.5. Comparison of SUV_{max} in Patients of Two Groups. The SUV_{max} values were compared in the two groups of patients, and the results are shown in Figure 6. It indicated that the SUV_{max} value of patients in the benign and malignant nodule group was 3.09 ± 0.36 and 8.74 ± 0.92, respectively. Thus, the SUV_{max} value of patients in group B was obviously lower in contrast to group M with statistical difference ($P < 0.01$).

Table 1: Basic information of patients with benign and malignant nodules.

Group	Male (cases (%))	Female (cases (%))	Age (years)	Size of TN (mm)
Group B	6 (37.5)	19 (45.24)	60.92 ± 11.11	24.05 ± 0.19
Group M	10 (62.5)	23 (54.76)	62.44 ± 12.06	19.02 ± 0.21
P value	0.77	0.65	0.092	0.073

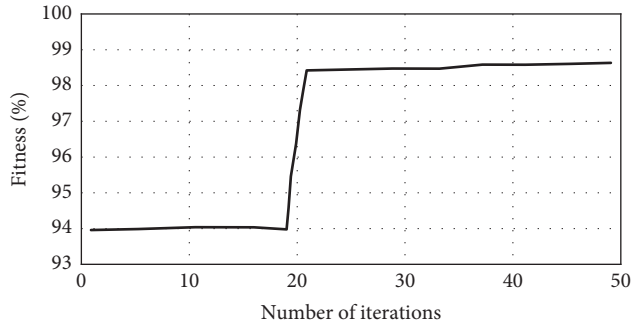

Figure 2: Fitness of the parameter optimization algorithm based on SVM.

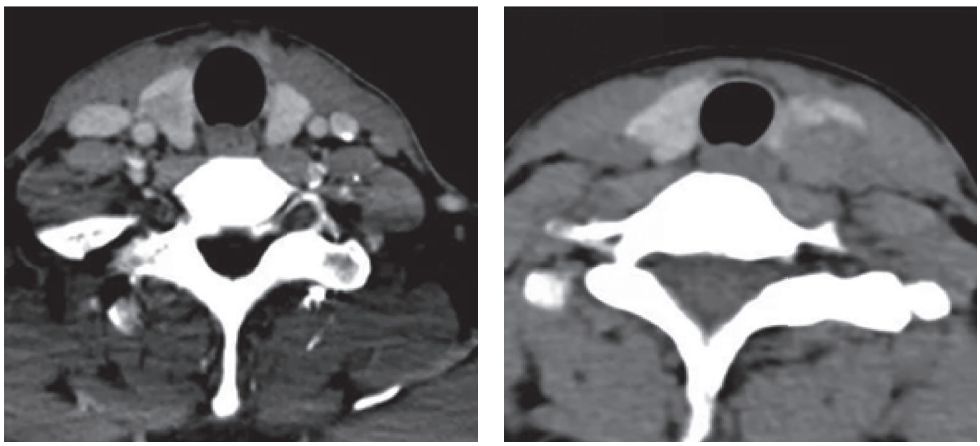

(a) (b)

Figure 3: PET-CT images of patients with benign TN (images of a female patient aged 43 years). (a) The plain CT and (b) enhanced CT images of a TN patient.

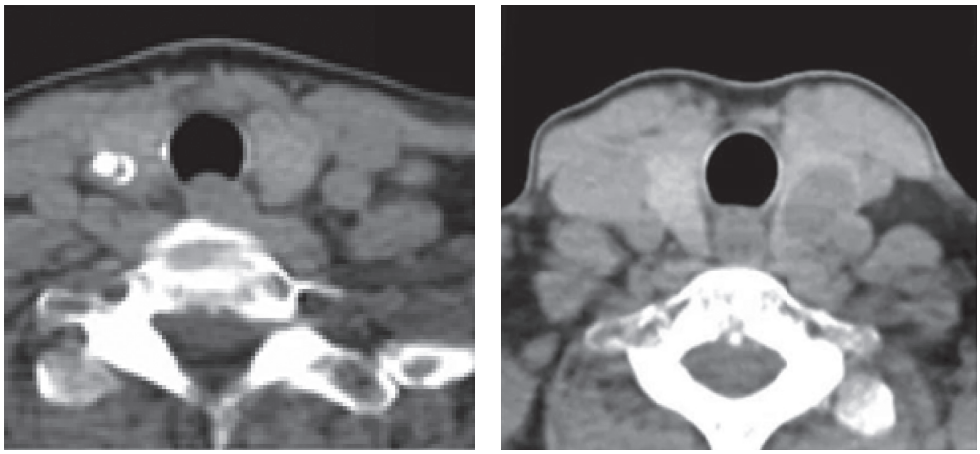

(a) (b)

Figure 4: PET-CT images of patients with malignant TN (images of a male patient aged 67 years). (a) The plain CT and (b) enhanced CT images of a thyroid cancer patient.

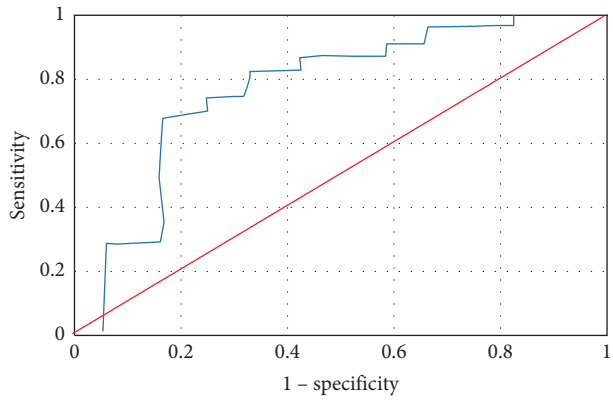

Figure 5: ROC curve for benign and malignant nodules diagnosed with SUV_{max}.

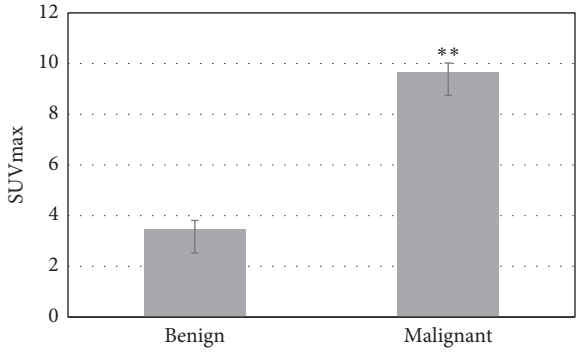

Figure 6: Comparison on SUV_{max} values for patients in two groups. Note: ** indicates dramatic difference in contrast to group B ($P < 0.01$).

3.6. PPIRs of RLN of Patients in Two Groups. After the two groups of patients were treated with thyroidectomy, the postoperative complications of the RLN injury were counted, and the results are illustrated in Figure 7. After treatment with the same method, the PPIR of RLN in group B and group M was 8% and 15.15%, respectively, one month after the surgery, that in groups B and M was 4% and 15.12%, respectively, two months after the surgery, and that was 0 and 9.09%, respectively, three months after the surgery. It suggested that the PPRI of RLN of malignant TN was higher than that of the benign TN, showing great difference ($P < 0.01$).

4. Discussion

Based on the SVM algorithm and the PSO algorithm, the parameters were optimized to adapt to the characteristics of TN. After the algorithm was optimized, its fitness was analyzed. The results showed that as the number of iterations increased, the fitness showed an increasing trend; the fitness level suddenly increased when the number of iterations was 19, and then remained at a stable level, with a fitness level of 98.3%. Gu et al. [12] mentioned in the research results of lung nodule classification after algorithm optimization that the higher the fitness, the greater the classification accuracy. Further analysis of the accuracy by taking the pathological

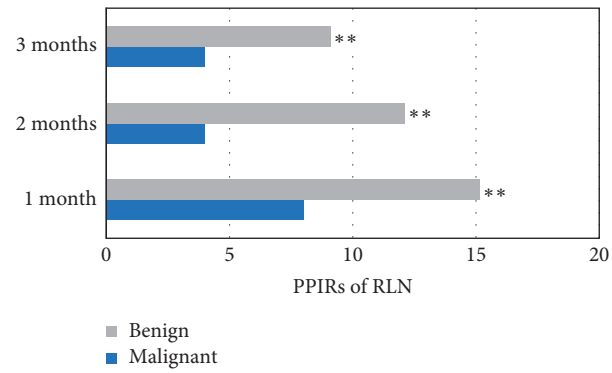

Figure 7: PPIRs of RLN of patients in two groups. Note: ** indicates obvious difference in contrast to group M ($P < 0.01$).

diagnosis result as the gold standard revealed that the accuracy rate of the optimized SVM algorithm reached 89% and 95.2% for malignant and benign classification of TN, respectively. The final classification accuracy could be 91.1%. These results showed that the PET-CT image classification method established based on the SVM algorithm in this study could avoid the randomness of artificial selection and the error caused by subjectivity in the clinical operation, and it had a good effect on the classification of TN.

Some research results showed that the benign and malignant TN had a reliable correlation with CT image characteristics [13, 14]. Moreover, PET/CT was used in more and more studies to diagnose patients, and the semiquantitative index SUV_{max} could be applied for the diagnosis and evaluation of benign and malignant nodules [15]. However, the current research results showed that there was still a partial overlap of SUV_{max} between benign and malignant nodules, making it highly controversial in the diagnosis of benign and malignant TN [16]. The results of SUV_{max} based on the SVM parameter optimization algorithm in this study suggested that the area under ROC was 0.795. When $SUV_{max} = 4.56$ was undertaken as the best critical point for diagnosis, the sensitivity and specificity of SUV_{max} for diagnosing the benign and malignant nodules was 81.33% and 76.18%, respectively. The results of Sollini et al. [17] showed that the SUV_{max} critical value for the diagnosis of benign and malignant TN was 5.0, and the corresponding diagnostic sensitivity and specificity was 60% and 91%, respectively. Thus, the sensitivity of SUV_{max} in the diagnosis of the benign and malignant nodules had been significantly improved, but its specificity was decreased to a certain degree. The SUV_{max} value of patients in group B was lower hugely than that of the patients in group M ($P < 0.01$), which was similar to the results of Małkowski et al. [18]. As the main motor nerve of the throat, the RLN was mainly responsible for the control of swallowing [19]. The degree of RLN injury was one of the indicators of the success of surgical treatment, and it was the most serious complication after TN [20]. The results of this study showed that the PPIR of RLN in the malignant TN group was higher in contrast to group B during the three months after the surgery, and the difference was dramatic ($P < 0.01$). A large number of research results had shown that PPIR of RLN was related to the benign and malignant

TN, the position of nodules, and the postoperative preventive measures [21]. The results of this study indicated that PPIR of RLN was observably correlated with benign and malignant TN, suggesting that the diagnosis of benign and malignant TN was of great meaningfulness in evaluating the PPIR of RLN in patients with TN.

5. Conclusion

The PSO algorithm was introduced based on the SVM algorithm so as to optimize the parameters of the SVM algorithm to enhance the classification accuracy and was applied to the clinical diagnosis of benign and malignant TN, so as to provide information on the occurrence of PPIR of RLN in TN patients. The results revealed that the proposed SVM algorithm improved the accuracy of the classification of TN greatly and could realize important significance in the evaluation of PPIR of RLN. However, there were some shortcomings in this study. The PPIR of RLN of the two groups of patients was counted, and the related factors of RLN injury were not further analyzed. In future work, the injury factors for RLN of TN patients will be analyzed to provide more accurate clinical guidance for postoperative injury assessment of RLN. In summary, the method established in this study achieved higher accuracy in the classification of TN based on the SVM parameter optimization algorithm, and it had a critical application value for the evaluation of PPIR of RLN.

Data Availability

The data used to support the findings of this study are available from the corresponding author upon request.

Conflicts of Interest

The authors declare no conflicts of interest.

Authors' Contributions

Jiyuan Wang and Hanqing Zou contributed equally to this work.

References

[1] R. Wong, S. G. Farrell, and M. Grossmann, "Thyroid nodules: diagnosis and management," *Medical Journal of Australia*, vol. 209, no. 2, pp. 92–98, 2018.

[2] J. H. Shin, J. H. Baek, J. Chung et al., "Ultrasonography diagnosis and imaging-based management of thyroid nodules: revised Korean society of thyroid radiology consensus statement and recommendations," *Korean Journal of Radiology*, vol. 17, no. 3, pp. 370–395, 2016.

[3] A. Gunn, T. Oyekunle, M. Stang, H. Kazaure, and R. Scheri, "Recurrent laryngeal nerve injury after thyroid surgery: an analysis of 11,370 patients," *Journal of Surgical Research*, vol. 255, pp. 42–49, 2020.

[4] W.-B. Yu and N.-S. Zhang, "Protection and dissection of recurrent laryngeal nerve in salvage thyroid cancer surgery to patients with insufficient primary operation extent and suspicious residual tumor," *Asian Pacific Journal of Cancer Prevention*, vol. 16, no. 17, pp. 7457–7461, 2015.

[5] F. Ben Bouallègue, Y. A. Tabaa, M. Kafrouni, G. Cartron, F. Vauchot, and D. Mariano-Goulart, "Association between textural and morphological tumor indices on baseline PET-CT and early metabolic response on interim PET-CT in bulky malignant lymphomas," *Medical Physics*, vol. 44, no. 9, pp. 4608–4619, 2017.

[6] L. K. Ferreira, J. M. Rondina, R. Kubo et al., "Support vector machine-based classification of neuroimages in Alzheimer's disease: direct comparison of FDG-PET, rCBF-SPECT and MRI data acquired from the same individuals," *Revista Brasileira de Psiquiatria*, vol. 40, no. 2, pp. 181–191, 2017.

[7] L. D'hulst, D. Van Weehaeghe, A Chiò et al., "Multicenter validation of [^{18}F]-FDG PET and support-vector machine discriminant analysis in automatically classifying patients with amyotrophic lateral sclerosis versus controls," *Amyotrophic Lateral Sclerosis and Frontotemporal Degeneration*, vol. 19, no. 7-8, pp. 570–577, 2018.

[8] X. Gao, C. Chu, Y. Li et al., "The method and efficacy of support vector machine classifiers based on texture features and multi-resolution histogram from 18F-FDG PET-CT images for the evaluation of mediastinal lymph nodes in patients with lung cancer," *European Journal of Radiology*, vol. 84, no. 2, pp. 312–317, 2015.

[9] G. Yin, Y. Song, X. Li et al., "Prediction of mediastinal lymph node metastasis based on 18F-FDG PET/CT imaging using support vector machine in non-small cell lung cancer," *European Radiology*, vol. 31, no. 6, pp. 3983–3992, 2020.

[10] R. Boostani and M. Sabeti, "Can evolutionary-based brain map be used as a complementary diagnostic tool with fMRI, CT and PET for schizophrenic patients?" *Journal of Biomedical Physics & Engineering*, vol. 7, no. 2, pp. 169–180, 2017.

[11] H. Cui, M. Shu, M. Song, and Y. Wang, "Parameter selection and performance comparison of particle swarm optimization in sensor networks localization," *Sensors*, vol. 17, no. 3, p. 487, 2017.

[12] Y. Gu, X. Lu, B. Zhang et al., "Automatic lung nodule detection using multi-scale dot nodule-enhancement filter and weighted support vector machines in chest computed tomography," *PLoS One*, vol. 14, no. 1, Article ID e0210551, 2019.

[13] M. Castellana, P. Trimboli, A. Piccardo, L. Giovanella, and G. Treglia, "Performance of 18F-fdg PET/CT in selecting thyroid nodules with indeterminate fine-needle aspiration cytology for surgery. a systematic review and a meta-analysis," *Journal of Clinical Medicine*, vol. 8, no. 9, p. 1333, 2019.

[14] F. E. Haydardedeoglu, G. S. Bagir, N. Torun, E. Kocer, M. Reyhan, and M. E. Ertorer, "Hounsfield unit value has null effect on thyroid nodules at 18F-FDG PET/CT scans," *Archives of Endocrinology and Metabolism*, vol. 62, no. 4, pp. 460–465, 2018.

[15] A. Piccardo, M. Puntoni, G. Treglia et al., "Thyroid nodules with indeterminate cytology: prospective comparison between 18F-FDG-PET/CT, multiparametric neck ultrasonography, 99mTc-MIBI scintigraphy and histology," *European Journal of Endocrinology*, vol. 174, no. 5, pp. 693–703, 2016.

[16] Y. Cheng, P. Wu, F. Du et al., "Diagnostic efficacy of (18)F-FDG PET-CT for focal hypermetabolic thyroid nodules," *Zhonghua Zhongliu Zazhi*, vol. 39, no. 10, pp. 759–763, 2017, in Chinese.

[17] M. Sollini, L. Cozzi, G. Pepe et al., "[18F]FDG-PET/CT texture analysis in thyroid incidentalomas: preliminary results," *European Journal of Hybrid Imaging*, vol. 1, no. 1, p. 3, 2017.

[18] B. Małkowski, Z. Serafin, R. Glonek, S. Suwała, R. Łopatto, and R. Junik, "The role of 18F-fdg PET/CT in the management of the autoimmune thyroid diseases," *Frontiers in Endocrinology*, vol. 10, p. 208, 2019.

[19] T. S. Wang and J. A. Sosa, "Thyroid surgery for differentiated thyroid cancer - recent advances and future directions," *Nature Reviews Endocrinology*, vol. 14, no. 11, pp. 670–683, 2018.

[20] G. Wu and K. Wang, "A novel variation of the recurrent laryngeal nerve," *BMC Surgery*, vol. 17, no. 1, p. 66, 2017.

[21] S. Wijerathne, X. Goh, and R. Parameswaran, "Ipsilateral nonrecurrent laryngeal nerve palsy and delayed palsy of the contralateral recurrent laryngeal nerve in a case of third-time reoperative thyroid surgery," *Annals of the Royal College of Surgeons of England*, vol. 101, no. 2, pp. e55–e58, 2019.